Author's accepted manuscript

Homogenization of porous thin films and perforated layers: Comparison of analytical and numerical approaches

Henning Richter

DOI:10.1016/j.mechmat.2015.06.010

To appear in: *Mechanics of Materials*

Homogenization of porous thin films and perforated layers: Comparison of analytical and numerical approaches

H. Richter[a,*]

[a]*Institute of Materials Research, German Aerospace Center (DLR), Linder Höhe, 51147 Cologne, Germany*

Abstract

The mechanical properties of porous thin films and perforated layers are affected by pore content, shape and arrangement. The experimental determination of the in-plane mechanical properties of such materials is challenging, yet reliable data are essential for materials development and component design. Analytical and numerical approaches therefore provide valuable, supplementary tools for evaluating the effect of porosity on the mechanical properties of such materials.

The applicability of both the classical self-consistent method and the Mori-Tanaka approach to the estimation of the effective elastic properties of porous thin films and perforated layers is investigated in this paper. For generic model microstructures with various arrangements of pores, variable pore content and varying matrix Poisson's ratio, the effective elastic properties predicted by the classical self-consistent method and by the Mori-Tanaka approach are quantitatively compared with results obtained by numerical experiments. Based upon this comparison, the range of validity of both the classical self-consistent method and the Mori-Tanaka approach with regard to the different arrangements of pores investigated is defined, and the deviation to be expected if critical values of pore content or inter-pore distance are exceeded and interactions between adjacent pores are occurring is assessed.

Keywords: Finite element method, Self-consistent method, Mori-Tanaka approach, Micromechanics, Porous thin films, Constitutive behaviour

*Corresponding author. Tel.: +49 2203 601-2430
Email address: henning.richter@dlr.de (H. Richter)

1. Introduction

Porous thin films and perforated layers are increasingly used in innovative engineering applications, for example as filters (Kuiper et al., 2002), functional coatings for sensing or catalytic reaction tasks (Van Noyen et al., 2011; Zander et al., 2007), semiconductors in microelectronic devices (Föll et al., 2002), packaging medium for micro-electromechanical systems (Zekry et al., 2010), or to assure the biocompatibility of implants (Buchko et al., 2001). Depending on the intended application, such materials exhibit a wide variability of volume fraction, shape and arrangement of pores, which in turn affects their mechanical properties (Chao et al., 2005; Ha et al., 2010; Jauffrés et al., 2011; Vanstreels, 2013). Understanding the relation between pore microstructure and effective mechanical properties therefore plays a key role in successfully implementing these materials in practice.

However, the direct experimental determination of the mechanical properties, such as Young's modulus and Poisson's ratio, of porous thin films and perforated layers involves implications: Mechanical indentation tests, which are commonly used to measure Young's modulus, are sensitive to indenter type, penetration depth and substrate influence (Ben-Nissan et al., 2013; Bhushan and Venkatesan, 2005; Hemmouche et al., 2013; Zhou et al., 2011). Due to the limited size of the effectively tested material volume, the local pore structure may seriously affect indentation test results (Vanstreels, 2013). Advanced optical or acoustic tests, which are used to determine Poisson's ratio, depend upon accurate density measurements and a detailed analysis of the test data to yield reliable results (Flannery et al., 2001; Zhou et al., 2011).

Against this background, analytical homogenization approaches provide valuable tools for accompanying the interpretation of test results and evaluating the effect of porosity on Young's modulus and Poisson's ratio of porous thin films and perforated layers, stimulating and speeding up the process of materials development and component design. To be of practical use, such approaches need to be able to accurately capture interaction effects arising from the particularly small inter-pore distances of these materials.

In the present paper, this issue is investigated with regard to both the classical self-consistent method (SCM) initially suggested by Hershey (1954) and Kröner (1958) and the Mori-Tanaka approach (MT) described by Tanaka and Mori (1972). The SCM and the MT represent analytical homogenization approaches capable of accounting for pore content and interaction effects between neighbouring pores, lending themselves to the computation

of the Young's and shear moduli and Poisson's ratios of porous thin films and perforated layers. To further advance the understanding of the impact of pore content and arrangement, as well as inter-pore distance, on the applicability of the SCM and the MT to the homogenization of such materials, the following open questions are addressed:

- How are porosity and inter-pore distance correlated?
- What are the intervals of porosity and inter-pore distance over which the SCM and the MT yield acceptable results?
- How does the Poisson's ratio of the bulk material influence the results of the SCM and the MT?

These questions were investigated in a series of numerical experiments on generic, planar microstructure models with circular pores. The microstructure models were generated by means of a specifically developed software tool, which allows to create virtual microstructures with varying pore content and arrangement. Microstructure models with square, rhombic and random arrangements of pores were studied in order to cover the range of pore configurations commonly found in reality.

In order to evaluate the validity of predictions obtained by the SCM and the MT, the effective elastic properties estimated by the SCM and the MT for different levels of porosity and varying Poisson's ratio of the bulk material were quantitatively compared with results obtained by finite element analyses of these microstructure models in conjunction with a numerical homogenization approach (Anthoine, 1995; Michel et al., 1999). To identify a correlation between porosity and inter-pore distance, the inter-pore distances of microstructure models with square and rhombic pore structure, as well as the average inter-pore distances of several thousand random microstructure models found by a Monte-Carlo simulation, were related to their pore content. These investigations led to clear guidelines on the applicability and range of validity of both the SCM and the MT with regard to the homogenization of porous thin films and perforated layers with square, rhombic and random pore configurations.

2. Analytical homogenization approach

In general terms, porous thin films and perforated layers represent a variant of inhomogeneous two-phase materials, which are composed of constituents with different mechanical properties, namely a matrix phase and

inclusions or, in the case of vanishing stiffness, pores. In order to treat such materials within the framework of continuum mechanics, the identification of their effective mechanical properties, which are governed by the volume fraction, shape, arrangement and mechanical properties of the constituent phases, is required. The effective elastic properties are commonly found by homogenization, which involves evaluating the mechanical response of a finite, generic section of the inhomogeneous material, a so-called Representative Volume Element (RVE) (Hill, 1963). In order to formulate the constitutive equation for the RVE domain, the complex local stress and strain fields within the constituent phases are calculated individually, and their contribution to the overall stress and strain state is accounted for by volume averaging. The resulting effective elasticity or compliance tensors represent an equivalent homogeneous continuum, which replaces the initial inhomogeneous microstructure of the RVE domain.

2.1. Basic relations

The main aspects of the analytical homogenization of porous thin films and perforated layers are outlined in this section. The following considerations are limited to linearly elastic materials that exhibit a matrix-inclusion-type microstructure with a homogeneous matrix domain Ω_m and an inclusion domain $\Psi = \bigcup_{i=1}^{n} \Psi_i$, which represents the union of n homogeneous inclusions, or, in the case of vanishing stiffness, pores Ψ_i distributed over Ω_m. The inclusions Ψ_i are assumed to be of similar shape and orientation and to have identical elastic properties. The domain $\Omega = \Omega_\mathrm{m} \cup \Psi$ constitutes a Representative Volume Element (RVE) of a porous thin film or perforated layer, as shown in Fig. 1.

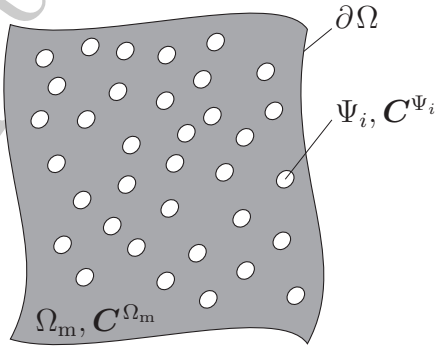

Figure 1: Schematic representation of a RVE for a porous thin film or perforated layer with matrix domain Ω_m and n homogeneous inclusions Ψ_i.

The constitutive equation of the the matrix phase reads

$$\overline{\boldsymbol{\sigma}}^{\Omega_\mathrm{m}} = \boldsymbol{C}^{\Omega_\mathrm{m}} : \overline{\boldsymbol{\varepsilon}}^{\Omega_\mathrm{m}}, \tag{1}$$

where the overbar denotes averaged quantities and $\boldsymbol{C}^{\Omega_\mathrm{m}}$ represents the elasticity tensor of the homogeneous matrix. The averages of stress $\overline{\boldsymbol{\sigma}}^{\Omega_\mathrm{m}}$ and strain $\overline{\boldsymbol{\varepsilon}}^{\Omega_\mathrm{m}}$ are defined as

$$\overline{\boldsymbol{\sigma}}^{\Omega_\mathrm{m}} = \frac{1}{V_{\Omega_\mathrm{m}}} \int\limits_{\Omega_\mathrm{m}} \boldsymbol{\sigma}^{\Omega_\mathrm{m}}(\boldsymbol{x})\, \mathrm{d}\Omega_\mathrm{m}, \tag{2}$$

$$\overline{\boldsymbol{\varepsilon}}^{\Omega_\mathrm{m}} = \frac{1}{V_{\Omega_\mathrm{m}}} \int\limits_{\Omega_\mathrm{m}} \boldsymbol{\varepsilon}^{\Omega_\mathrm{m}}(\boldsymbol{x})\, \mathrm{d}\Omega_\mathrm{m} \tag{3}$$

within the matrix volume V_{Ω_m} of unit thickness (Hill, 1963). In analogy to Eq. (1), the constitutive equation of the merged inclusion phase is given by

$$\overline{\boldsymbol{\sigma}}^{\Psi} = \boldsymbol{C}^{\Psi} : \overline{\boldsymbol{\varepsilon}}^{\Psi}. \tag{4}$$

The effective elasticity tensor $\overline{\boldsymbol{C}}^{\mathrm{eff}}$ of the two-phase material can be derived from the overall constitutive equation of the RVE

$$\overline{\boldsymbol{\sigma}} = \overline{\boldsymbol{C}}^{\mathrm{eff}} : \overline{\boldsymbol{\varepsilon}}. \tag{5}$$

The overall stress tensor $\overline{\boldsymbol{\sigma}}$ is equal to the sum of the volume-averaged stresses within the matrix and inclusion phase,

$$\overline{\boldsymbol{\sigma}} = \varphi_{\Omega_\mathrm{m}}\, \overline{\boldsymbol{\sigma}}^{\Omega_\mathrm{m}} + \varphi_{\Psi}\, \overline{\boldsymbol{\sigma}}^{\Psi}, \tag{6}$$

where $\varphi_{\Omega_\mathrm{m}}$ and φ_{Ψ} denote the volume fraction of the matrix and of the inclusion phase. Similarly, the overall strain tensor $\overline{\boldsymbol{\varepsilon}}$ is given by

$$\overline{\boldsymbol{\varepsilon}} = \varphi_{\Omega_\mathrm{m}}\, \overline{\boldsymbol{\varepsilon}}^{\Omega_\mathrm{m}} + \varphi_{\Psi}\, \overline{\boldsymbol{\varepsilon}}^{\Psi}, \tag{7}$$

cf. Hill (1963). Using Eqs. (4) and (5), Eq. (6) can be rewritten as

$$\overline{\boldsymbol{C}}^{\mathrm{eff}} : \overline{\boldsymbol{\varepsilon}} = \varphi_{\Omega_\mathrm{m}}\, \overline{\boldsymbol{\sigma}}^{\Omega_\mathrm{m}} + \varphi_{\Psi}\, \boldsymbol{C}^{\Psi} : \overline{\boldsymbol{\varepsilon}}^{\Psi}, \tag{8}$$

and with Eq. (1), Eq. (7) reads

$$\boldsymbol{C}^{\Omega_\mathrm{m}} : \overline{\boldsymbol{\varepsilon}} = \varphi_{\Omega_\mathrm{m}}\, \overline{\boldsymbol{\sigma}}^{\Omega_\mathrm{m}} + \varphi_{\Psi}\, \boldsymbol{C}^{\Omega_\mathrm{m}} : \overline{\boldsymbol{\varepsilon}}^{\Psi}. \tag{9}$$

Subtracting Eq. (9) from Eq. (8) leads to

$$\overline{\boldsymbol{C}}^{\mathrm{eff}} : \overline{\boldsymbol{\varepsilon}} = \boldsymbol{C}^{\Omega_\mathrm{m}} : \overline{\boldsymbol{\varepsilon}} + \varphi_{\Psi}\, (\boldsymbol{C}^{\Psi} - \boldsymbol{C}^{\Omega_\mathrm{m}}) : \overline{\boldsymbol{\varepsilon}}^{\Psi}, \tag{10}$$

which can be solved for the effective elasticity tensor $\overline{\boldsymbol{C}}^{\mathrm{eff}}$ of the equivalent homogeneous material if the strain $\overline{\boldsymbol{\varepsilon}}^{\Psi}$ in the inclusion phase Ψ is known.

2.2. Classical self-consistent method

An analytical solution for $\overline{\boldsymbol{\varepsilon}}^{\Psi}$ can be found by considering a single inclusion Ψ_i embedded in an infinite homogeneous matrix. Within the framework of the SCM, the elastic properties of the homogeneous matrix phase are assumed to be equal to the unknown overall elastic properties of the two-phase material in order to account for interactions between adjacent inclusions (Budiansky, 1965; Hershey, 1954; Hill, 1965; Kröner, 1958). For an ellipsoidal inclusion Ψ_i under a prescribed overall strain $\overline{\boldsymbol{\varepsilon}}$, the inclusion strain $\overline{\boldsymbol{\varepsilon}}^{\Psi}$ is then found by applying Eshelby's equivalent inclusion method,

$$\overline{\boldsymbol{\varepsilon}}^{\Psi} = \overline{\boldsymbol{A}}_{\mathrm{SCM}} : (\overline{\boldsymbol{A}}_{\mathrm{SCM}} - \overline{\boldsymbol{S}})^{-1} : \overline{\boldsymbol{\varepsilon}}, \tag{11}$$

where $\overline{\boldsymbol{A}}_{\mathrm{SCM}}$ is defined as

$$\overline{\boldsymbol{A}}_{\mathrm{SCM}} = (\overline{\boldsymbol{C}}^{\mathrm{eff}} - \boldsymbol{C}^{\Psi})^{-1} : \overline{\boldsymbol{C}}^{\mathrm{eff}} \tag{12}$$

and $\overline{\boldsymbol{S}}$ denotes the effective Eshelby tensor (Eshelby, 1957). Inserting Eqs. (11) and (12) into Eq. (10) yields the implicit relation

$$\overline{\boldsymbol{C}}^{\mathrm{eff}}_{\mathrm{SCM}} = \boldsymbol{C}^{\Omega_{\mathrm{m}}} - \varphi_{\Psi} \boldsymbol{C}^{\Omega_{\mathrm{m}}} : (\boldsymbol{I} - \overline{\boldsymbol{S}})^{-1} \tag{13}$$

for the effective elasticity tensor of a porous two-phase material with $\boldsymbol{C}^{\Psi} = \boldsymbol{0}$.

2.3. Mori-Tanaka approach

Within the framework of the MT, the inclusion Ψ_i is assumed to be subjected to an average matrix stress or strain composed of the applied overall stress or strain and stress or strain fluctuations caused by the presence of other inclusions (Benveniste, 1987; Mori and Tanaka, 1973; Tanaka and Mori, 1972; Weng, 1984). Then, the inclusion strain $\overline{\boldsymbol{\varepsilon}}^{\Psi}$ is given by

$$\overline{\boldsymbol{\varepsilon}}^{\Psi} = \boldsymbol{A}_{\mathrm{MT}} : [(1 - \varphi_{\Psi})\boldsymbol{I} + \varphi_{\Psi} \boldsymbol{A}_{\mathrm{MT}}]^{-1} : \overline{\boldsymbol{\varepsilon}}, \tag{14}$$

where $\boldsymbol{A}_{\mathrm{MT}}$ is defined by Benveniste (1987) as

$$\boldsymbol{A}_{\mathrm{MT}} = \left[\boldsymbol{I} + \boldsymbol{S} : \boldsymbol{C}^{\Omega_{\mathrm{m}}{}^{-1}} : (\boldsymbol{C}^{\Psi} - \boldsymbol{C}^{\Omega_{\mathrm{m}}})\right]^{-1} \tag{15}$$

and $\boldsymbol{S}$ is the Eshelby tensor. With Eqs. (14) and (15), Eq. (10) can be written as

$$\overline{\boldsymbol{C}}^{\mathrm{eff}}_{\mathrm{MT}} = \boldsymbol{C}^{\Omega_{\mathrm{m}}} - \varphi_{\Psi} \boldsymbol{C}^{\Omega_{\mathrm{m}}} : [\boldsymbol{I} - (1 - \varphi_{\Psi})\boldsymbol{S}]^{-1} \tag{16}$$

for a porous two-phase material.

2.4. Solution for porous thin films and perforated layers

In order to analytically determine the effective elastic constants of porous thin films and perforated layers, the plane stress formulations of Eqs. (13) and (16) are derived in the following. They can be conveniently formulated by introducing two base tensors $\boldsymbol{B}^1$ and $\boldsymbol{B}^2$ (Hill, 1965; Nemat-Nasser and Hori, 1999),

$$B^1_{ijkl} = \frac{1}{2}\,\delta_{ij}\,\delta_{kl} \quad \text{and} \tag{17}$$

$$B^2_{ijkl} = -\frac{1}{2}\,\delta_{ij}\,\delta_{kl} + \frac{1}{2}\,(\delta_{ik}\,\delta_{jl} + \delta_{il}\,\delta_{jk}), \tag{18}$$

which satisfy the relations

$$\boldsymbol{B}^1 : \boldsymbol{B}^1 = \boldsymbol{B}^1, \tag{19}$$

$$\boldsymbol{B}^2 : \boldsymbol{B}^2 = \boldsymbol{B}^2 \quad \text{and} \tag{20}$$

$$\boldsymbol{B}^1 : \boldsymbol{B}^2 = \boldsymbol{B}^2 : \boldsymbol{B}^1 = \boldsymbol{0}. \tag{21}$$

In Eqs. (17) and (18), δ_{ij} denotes the Kronecker symbol with $i, j, k, l = 1, 2$ for plane stress. Then, the elasticity tensor $\boldsymbol{C}^{\Omega_\mathrm{m}}$ of the homogeneous, isotropic matrix domain Ω_m can be written as

$$\boldsymbol{C}^{\Omega_\mathrm{m}} = \frac{E_\mathrm{m}}{1-\nu_\mathrm{m}}\,\boldsymbol{B}^1 + \frac{E_\mathrm{m}}{1+\nu_\mathrm{m}}\,\boldsymbol{B}^2 \tag{22}$$

for plane stress, where E_m and ν_m denote the Young's modulus and the Poisson's ratio of the matrix, respectively. Similarly, the effective elasticity tensor $\overline{\boldsymbol{C}}^{\mathrm{eff}}$ of the equivalent homogeneous material can be expressed as

$$\overline{\boldsymbol{C}}^{\mathrm{eff}} = \frac{\overline{E}}{1-\overline{\nu}}\,\boldsymbol{B}^1 + \frac{\overline{E}}{1+\overline{\nu}}\,\boldsymbol{B}^2, \tag{23}$$

assuming that the overall elastic behaviour of the porous thin film or perforated layer is isotropic due to a homogeneous distribution of pores. Here, $\overline{E}$ and $\overline{\nu}$ are the effective Young's modulus and the effective Poisson's ratio, respectively. The two-dimensional effective Eshelby tensor $\overline{\boldsymbol{S}}$ can be derived from the Eshelby tensor for cylindrical pore geometry. Using the two base tensors $\boldsymbol{B}^1$ and $\boldsymbol{B}^2$, $\overline{\boldsymbol{S}}$, whose entries only depend on the unknown effective Poisson's ratio $\overline{\nu}$ of the equivalent homogeneous material, can be written as

$$\overline{\boldsymbol{S}} = \frac{1+\overline{\nu}}{2}\,\boldsymbol{B}^1 + \frac{3-\overline{\nu}}{4}\,\boldsymbol{B}^2, \tag{24}$$

cf. Nemat-Nasser and Hori (1999).

With regard to the SCM, using Eqs. (22), (23) and (24), the plane stress formulation of Eq. (13) in terms of the base tensors $\boldsymbol{B}^1$ and $\boldsymbol{B}^2$ reads

$$\overline{\boldsymbol{C}}^{\text{eff}}_{\text{SCM}} = \frac{E_\text{m}}{1-\nu_\text{m}}\left[1-\varphi_\Psi\left(1-\frac{1+\overline{\nu}_{\text{SCM}}}{2}\right)^{-1}\right]\boldsymbol{B}^1 + \frac{E_\text{m}}{1+\nu_\text{m}}\left[1-\varphi_\Psi\left(1-\frac{3-\overline{\nu}_{\text{SCM}}}{4}\right)^{-1}\right]\boldsymbol{B}^2 \,. \quad (25)$$

Comparison of the coefficients of the base tensors $\boldsymbol{B}^1$ and $\boldsymbol{B}^2$ leads to a system of equations,

$$\frac{\overline{E}_{\text{SCM}}}{E_\text{m}} = \frac{1-\overline{\nu}_{\text{SCM}}}{1-\nu_\text{m}}\left[1-\varphi_\Psi\left(1-\frac{1+\overline{\nu}_{\text{SCM}}}{2}\right)^{-1}\right], \quad (26)$$

$$\frac{\overline{E}_{\text{SCM}}}{E_\text{m}} = \frac{1+\overline{\nu}_{\text{SCM}}}{1+\nu_\text{m}}\left[1-\varphi_\Psi\left(1-\frac{3-\overline{\nu}_{\text{SCM}}}{4}\right)^{-1}\right], \quad (27)$$

from which the following relations for the effective Young's modulus $\overline{E}_{\text{SCM}}$ and Poisson's ratio $\overline{\nu}_{\text{SCM}}$ for plane stress conditions are obtained:

$$\frac{\overline{E}_{\text{SCM}}}{E_\text{m}} = 1-3\varphi_\Psi\,, \quad (28)$$

$$\frac{\overline{\nu}_{\text{SCM}}}{\nu_\text{m}} = 1-\varphi_\Psi\left(3-\frac{1}{\nu_\text{m}}\right). \quad (29)$$

The effective shear modulus $\overline{G}_{\text{SCM}}$ is then found using the relation

$$\overline{G}_{\text{SCM}} = \frac{\overline{E}_{\text{SCM}}}{2(1+\overline{\nu}_{\text{SCM}})} \quad (30)$$

for overall isotropic material behaviour.

For the MT, the effective Young's modulus $\overline{E}_{\text{MT}}$ and Poisson's ratio $\overline{\nu}_{\text{MT}}$ for plane stress conditions can be found analogously from Eq. (16) with the two-dimensional Eshelby tensor $\boldsymbol{S}$, cf. Barai and Weng (2011):

$$\frac{\overline{E}_{\text{MT}}}{E_\text{m}} = \frac{1-\varphi_\Psi}{1+2\varphi_\Psi}\,, \quad (31)$$

$$\overline{\nu}_{\text{MT}} = \frac{(1-\varphi_\Psi)\nu_\text{m}+\varphi_\Psi}{1+2\varphi_\Psi}\,. \quad (32)$$

3. Numerical homogenization approach

It is well-known, and obvious from Eq. (28), that, for plane stress problems such as those found in porous thin films and perforated layers, the SCM is only defined on the interval from 0 to 1/3 total pore content and predicts the effective elastic moduli to vanish at higher porosities (Markov, 2000; Nemat-Nasser and Hori, 1999; Torquato, 2006). Over this interval, the inter-pore distances gradually shorten, leading to growing interactions between the stress and strain fields of adjacent pores. Using discrete models of the pore microstructure, these complex, interacting local fields can be computed via the finite element method (FEM).

3.1. Numerical model

To investigate the effect of inter-pore interactions and to establish a reference with which predictions obtained by the SCM and the MT can be compared, numerical experiments on two-dimensional RVEs with varying pore content, as well as with different arrangements of pores, were carried out. In extension of previous studies (Cabrillac et al., 1998; Day et al., 1992; Hu et al., 2000; Khatam et al., 2009; Xie and Fan, 2010), comparatively large RVEs with square, rhombic and random configurations of circular pores under periodic boundary conditions were investigated.

RVEs with square pore structure were generated by positioning discs with uniform radius r equidistantly on a lattice and performing a Boolean operation to cut circular pores out of the RVE domain Ω. Similarly, RVEs with rhombic pore configuration were created by using two lattices, which were offset against each other by half the inter-pore distance in both lattice directions. The rhombic pattern resembles a hexagonal arrangement, which cannot be replicated periodically within a square RVE domain. RVEs with random pore configurations were generated by means of a random sequential addition algorithm (Widom, 1966): Discs with uniform radius and a minimum distance of 10 % of their diameter were sequentially cut out of the RVE domain, until the predefined level of porosity was reached. In all cases, a small band of matrix material was preserved at the perimeter of the RVEs to ensure mesh periodicity.

The above approaches were implemented in a software tool to allow for an automated generation of virtual microstructures with varying amounts of porosity, as illustrated in Fig. 2. The commercial finite element software package Abaqus (Dassault Systèmes, 2010) was used for the subsequent

finite element analyses of the RVEs. All RVEs were meshed with second-order, plane stress quadrilateral elements. The optimum element size was found by mesh convergence studies.

3.2. Computation of effective elastic constants

In order to compute its overall elastic response, each RVE was subjected to three independent deformation states, two cases of uniaxial deformation $\overline{\boldsymbol{\varepsilon}}^{\mathrm{I}}$ and $\overline{\boldsymbol{\varepsilon}}^{\mathrm{II}}$ and a case of pure shear $\overline{\boldsymbol{\varepsilon}}^{\mathrm{VI}}$ under plane stress conditions,

$$\overline{\boldsymbol{\varepsilon}}^{\mathrm{I}} = \begin{bmatrix} \varepsilon_{\mathrm{a}} \\ 0 \\ 0 \end{bmatrix}, \qquad \overline{\boldsymbol{\varepsilon}}^{\mathrm{II}} = \begin{bmatrix} 0 \\ \varepsilon_{\mathrm{a}} \\ 0 \end{bmatrix}, \qquad \overline{\boldsymbol{\varepsilon}}^{\mathrm{VI}} = \begin{bmatrix} 0 \\ 0 \\ \frac{1}{2}\varepsilon_{\mathrm{a}} \end{bmatrix}, \tag{33}$$

with a given strain component ε_{a} (Zohdi and Wriggers, 2005). Periodic boundary conditions were imposed on the edges of the RVEs to emulate the compliance of the surrounding material (Huet, 1990; Michel et al., 1999; Terada et al., 2000). The resulting shear stress fields within exemplary RVEs with different pore configurations under prescribed overall strain $\overline{\boldsymbol{\varepsilon}}^{\mathrm{VI}}$ with $\varepsilon_{\mathrm{a}} = 0.001$ are shown in Fig. 2. For the homogeneous matrix domain Ω_{m} of the RVEs, isotropic material behaviour with Young's modulus $E_{\mathrm{m}} = 380\,\mathrm{GPa}$ and Poisson's ratio $\nu_{\mathrm{m}} = 0.22$ was assumed. These values are characteristic for aluminium oxide (Morrell, 1985).

For each predefined deformation state $\overline{\boldsymbol{\varepsilon}}$, the overall stresses $\overline{\boldsymbol{\sigma}}$ were then obtained by averaging the resulting stresses $\boldsymbol{\sigma}(\boldsymbol{x}_{\mathrm{IP}_i})$ at the integration points of the n finite elements,

$$\overline{\boldsymbol{\sigma}} \approx \frac{1}{A_\Omega} \sum_{i=1}^{n} \boldsymbol{\sigma}(\boldsymbol{x}_{\mathrm{IP}_i})\, A_{\mathrm{IP}_i}\,, \tag{34}$$

where A_Ω denotes the area of the RVE domain Ω, and A_{IP_i} is the area associated with integration point i (Anthoine, 1995; Böhm, 2011; Hill, 1963). Using the overall stress-strain relation, which reads

$$\begin{bmatrix} \overline{\sigma}_{11} \\ \overline{\sigma}_{22} \\ \overline{\sigma}_{12} \end{bmatrix} = \begin{bmatrix} \overline{C}_{11}^{\mathrm{eff}} & \overline{C}_{12}^{\mathrm{eff}} & \overline{C}_{16}^{\mathrm{eff}} \\ \overline{C}_{21}^{\mathrm{eff}} & \overline{C}_{22}^{\mathrm{eff}} & \overline{C}_{26}^{\mathrm{eff}} \\ \overline{C}_{61}^{\mathrm{eff}} & \overline{C}_{62}^{\mathrm{eff}} & \overline{C}_{66}^{\mathrm{eff}} \end{bmatrix} \begin{bmatrix} \overline{\varepsilon}_{11} \\ \overline{\varepsilon}_{22} \\ 2\,\overline{\varepsilon}_{12} \end{bmatrix} \tag{35}$$

for plane stress conditions, the nine components of the effective elasticity matrix $\overline{\boldsymbol{C}}^{\mathrm{eff}}$ of each RVE were computed. Assuming that the homogenized

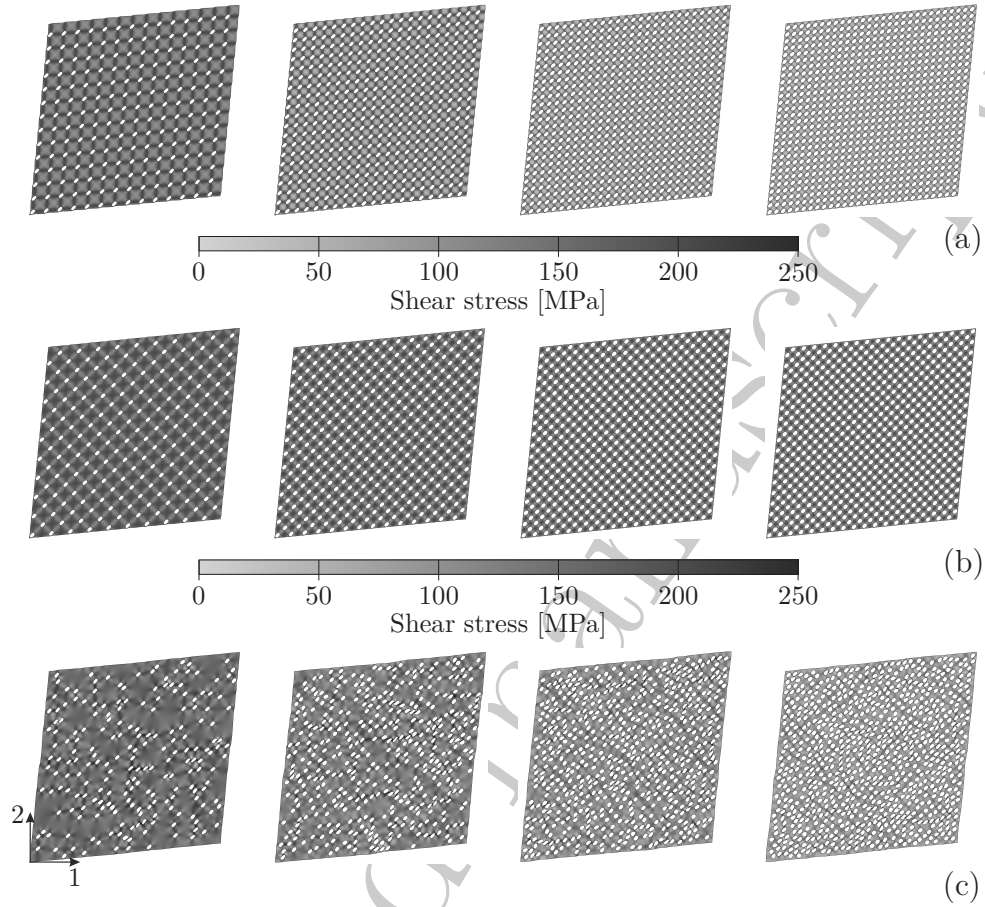

Figure 2: In-plane shear stress fields within RVEs of unit thickness with (a) periodic square arrangements of pores with 9.6 %, 19.6 %, 30.7 % and 38.5 % porosity, (b) periodic rhombic arrangements of pores with 9.8 %, 19.2 %, 28.4 % and 31.8 % porosity and (c) random arrangements of pores with 10 %, 20 %, 30 % and 40 % porosity. All RVEs were subjected to pure shear deformation under periodic boundary conditions (plots are scaled by a factor of 200). It is noted that considerably smaller RVEs might be used to represent domains with ordered square and rhombic pore arrangements. However, the RVE size was kept equal to facilitate automated RVE generation.

material exhibits at least two orthogonal planes of symmetry, as implied by prescribing three independent deformation states $\overline{\boldsymbol{\varepsilon}}^{\mathrm{I}}$, $\overline{\boldsymbol{\varepsilon}}^{\mathrm{II}}$ and $\overline{\boldsymbol{\varepsilon}}^{\mathrm{VI}}$ at the

boundary of the square RVE domain Ω, Eq. (35) can be written as

$$\begin{bmatrix} \overline{\sigma}_{11} \\ \overline{\sigma}_{22} \\ \overline{\sigma}_{12} \end{bmatrix} = \begin{bmatrix} \frac{\overline{E}_{11}}{1-\overline{\nu}_{12}\overline{\nu}_{21}} & \frac{\overline{\nu}_{21}\overline{E}_{11}}{1-\overline{\nu}_{12}\overline{\nu}_{21}} & 0 \\ \frac{\overline{\nu}_{12}\overline{E}_{22}}{1-\overline{\nu}_{12}\overline{\nu}_{21}} & \frac{\overline{E}_{22}}{1-\overline{\nu}_{12}\overline{\nu}_{21}} & 0 \\ 0 & 0 & \overline{G}_{12} \end{bmatrix} \begin{bmatrix} \overline{\varepsilon}_{11} \\ \overline{\varepsilon}_{22} \\ 2\,\overline{\varepsilon}_{12} \end{bmatrix}, \tag{36}$$

from which the effective Young's moduli $\overline{E}_{11}$ and $\overline{E}_{22}$, the effective shear modulus $\overline{G}_{12}$ and the effective Poisson's ratio $\overline{\nu}_{12}$ of each RVE were finally obtained. The effective Poisson's ratio $\overline{\nu}_{21}$ was then found using the relation

$$\overline{\nu}_{21} = \frac{\overline{E}_{22}}{\overline{E}_{11}}\,\overline{\nu}_{12} \tag{37}$$

for orthotropic material behaviour.

3.3. Determination of RVE size

In order to ensure that the RVEs yield effective elastic constants within reasonable tolerance limits, the appropriate RVE size was determined in a parametric study: Square RVEs with random arrangements of pores and different edge lengths l_Ω but fixed levels of porosity of 10 % and 30 %, respectively, were evaluated. Due to computational restrictions, the maximum RVE edge length was limited to $l_\Omega = 800\,\mathrm{mm}$. The components of the elasticity matrix $\overline{\boldsymbol{C}}$ of each RVE were computed according to the procedure described in the previous section.

Fig. 3 depicts the resulting overall elastic constants $\overline{C}_{ij}$, plotted against the RVE edge length l_Ω. The graphs show that the overall elastic constants converge to the effective ones with increasing RVE edge length. The relative differences d_r between the elastic constants computed for a RVE edge length of $l_\Omega = 400\,\mathrm{mm}$ and the corresponding quantities obtained for the largest RVE with $l_\Omega = 800\,\mathrm{mm}$,

$$d_\mathrm{r} = \left|\frac{\overline{C}_{ij}(l_\Omega = 400\,\mathrm{mm})}{\overline{C}_{ij}(l_\Omega = 800\,\mathrm{mm})} - 1\right|, \tag{38}$$

are less than 1 % for RVEs with 10 % porosity, and below 2 % for RVEs with 30 % porosity, cf. Fig. 3. From these results, a RVE edge length of $l_\Omega = 400\,\mathrm{mm}$ was chosen for the subsequent finite element analyses. This RVE edge length was kept equal for all pore configurations to allow for an automated generation and evaluation of the RVEs.

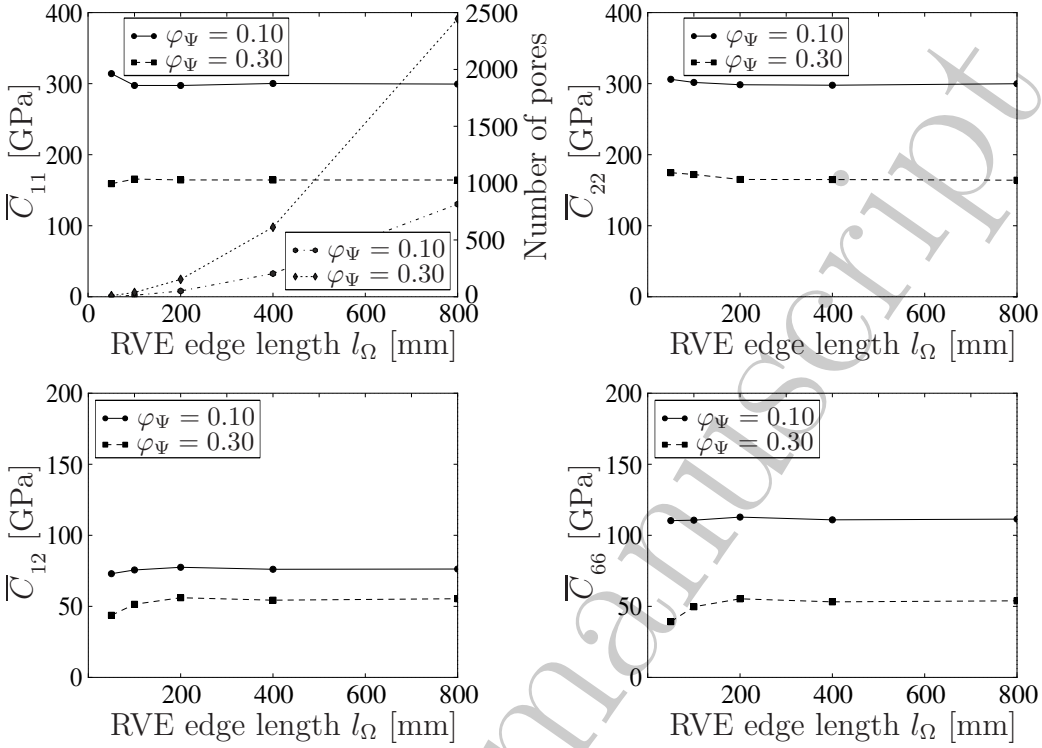

Figure 3: Dependence of the overall quantities $\overline{C}_{ij}$ on RVE edge length.

4. Results and discussion

For two-dimensional RVEs with porosity levels ranging from 0 % to 40 %, the effective elastic constants were computed using both the classical self-consistent method (SCM) and the Mori-Tanaka approach (MT), as well as the finite element method (FEM). With the SCM, the effective elastic moduli and the effective Poisson's ratio were obtained from Eqs. (28), (30) and (29) for overall isotropic material behaviour. With the MT, Eqs. (31), (32) and the corresponding form of Eq. (30) were used. In the numerical experiments, the effective elastic constants of the RVEs were evaluated in increments of approximately 5 % porosity, following the procedure described in Section 3.2. At each level of porosity, a RVE with both square and rhombic pore structure, and five different RVEs with random configurations of pores were analysed.

4.1. Effect of porosity

The effect of porosity on the validity of the SCM and MT estimates was evaluated by comparing the effective elastic constants predicted by both the SCM and the MT with the results of the numerical experiments on RVEs with varying levels of porosity and different pore configurations. Fig. 4 shows the resulting elastic constants, plotted against the porosity φ_Ψ. The results obtained from the numerical experiments on RVEs with square, rhombic and random arrangements of pores are marked by '$\curlywedge$', '$\times$' and '+', respectively.

The porosity dependence of the normalised Young's modulus $\overline{E}/E_\mathrm{m}$ is plotted in Fig. 4(a). For RVEs with square and rhombic pore configurations, the effective Young's moduli in 1- and 2-direction are equal, $\overline{E}_{11} = \overline{E}_{22}$. For RVEs with random pore configurations, the effective Young's moduli in 1- and 2-direction are similar, the relative difference between the values of $\overline{E}_{11}$ and $\overline{E}_{22}$ being 1.9 % at most. For clarity, the arithmetic means of the effective Young's moduli $\overline{E}_{11}$ and $\overline{E}_{22}$ are therefore used.

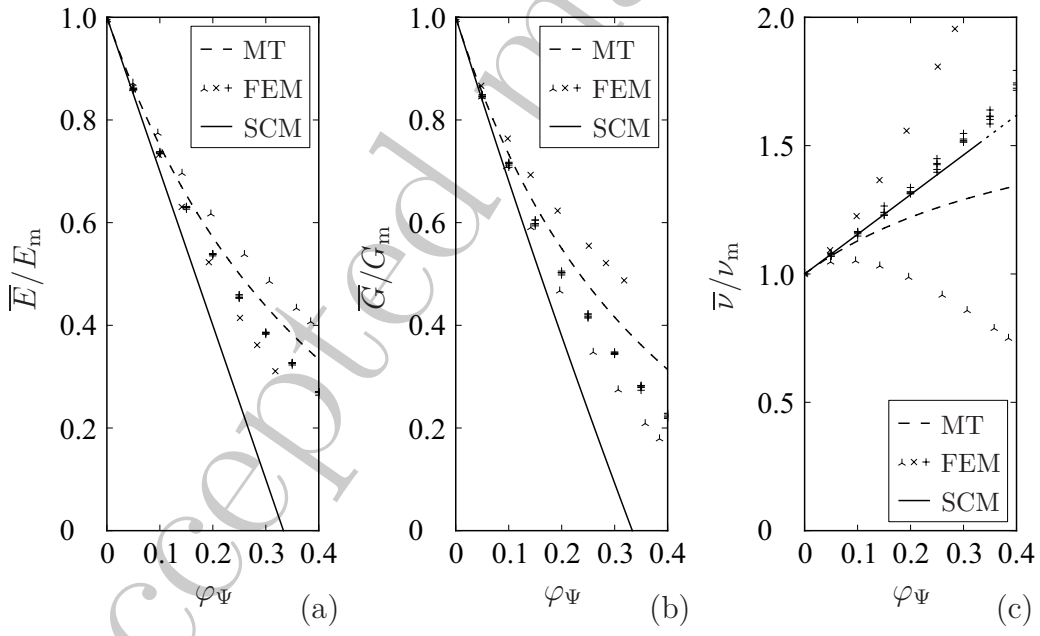

Figure 4: Comparison of the effective elastic constants obtained by the classical self-consistent method (SCM), the Mori-Tanaka approach (MT) and by finite element analyses (FEM) for RVEs with square ('$\curlywedge$'), rhombic ('$\times$') and random ('+') configurations of pores.

For low levels of porosity, the SCM predictions for the effective Young's modulus match the results of the numerical experiments, particularly for RVEs with rhombic and random pore arrangements. The MT estimates show much better agreement, irrespective of the RVEs' pore configuration. Among the pore configurations investigated, RVEs with square pore structure exhibit the highest tensile stiffness, which is attributed to the width of the load carrying ligaments between the pores.

With regard to the normalised shear modulus $\overline{G}/G_{\mathrm{m}}$ plotted in Fig. 4(b), the results reveal a similar trend. The relative differences between the SCM estimates and the FEM results are largest for RVEs with rhombic pore structure. This pore structure, which results from rotating the square pore configuration by 45°, yields the highest shear stiffness. For RVEs with random pore configurations, the relation $\overline{C}_{66} \approx (\overline{C}_{11} - \overline{C}_{12})/2$ approximately holds true: The relative difference between the values of $\overline{C}_{66}$ computed by this relation and those found independently from the pure shear deformation state $\overline{\boldsymbol{\varepsilon}}^{\mathrm{VI}}$ is 2.2 % on average and 9.6 % at most, indicating that the overall elastic behaviour of the RVEs with random arrangements of pores is indeed approximately isotropic.

From Eq. (28), it follows that the effective Young's modulus $\overline{E}$ and, consequently, the effective shear modulus $\overline{G}$ vanish at a porosity of $\varphi_\Psi = 1/3$, as already indicated in Section 3. This is in contradiction to the results of the numerical experiments: An RVE used for the finite element analyses will lose its stiffness if the concentration of pores is so high that overlapping of pores has to be permitted in order to further increase the RVE's porosity. In this case, adjacent pores may coalesce and the coherence of the matrix phase may be lost. However, this will not occur before reaching the jamming limit, which is $\varphi_\Psi = \pi/4$ for square and rhombic, and $\varphi_\Psi \approx 0.547$ for random distributions of circular pores within a square domain (Hinrichsen et al., 1986).

The dependence of the normalised Poisson's ratio $\overline{\nu}/\nu_{\mathrm{m}}$ on porosity is depicted in Fig. 4(c). For the specified matrix Poisson's ratio $\nu_{\mathrm{m}} = 0.22$, the predictions of the SCM and the results of the numerical experiments on RVEs with random pore structure are in good agreement over the entire range of porosity investigated, with a maximum relative difference of approximately 4 % at $\varphi_\Psi = 0.3$. The predictions of the MT deviate from the results of the numerical experiments by more than 5 % if a porosity level of $\varphi_\Psi = 0.15$ is exceeded. The situation is different for RVEs with ordered pore configurations: For the square pore structure, the effective Poisson's

ratio decreases with increasing porosity, a trend that has also been observed by Khatam et al. (2009) using unit cell models with a single circular pore and the finite-volume direct averaging micromechanics theory. For RVEs with rhombic pore structure, in contrast, the effective Poisson's ratio grows rapidly with increasing porosity.

4.2. Correlation between porosity and inter-pore distances

An increase in porosity of the RVEs goes along with a decrease of inter-pore distances, amplifying interactions between adjacent pores. For RVEs with random arrangements of pores, the correlation between porosity and inter-pore distances is illustrated by Fig. 5(a), which shows the frequency polygons of the nearest-neighbour inter-pore distances for different porosity levels.

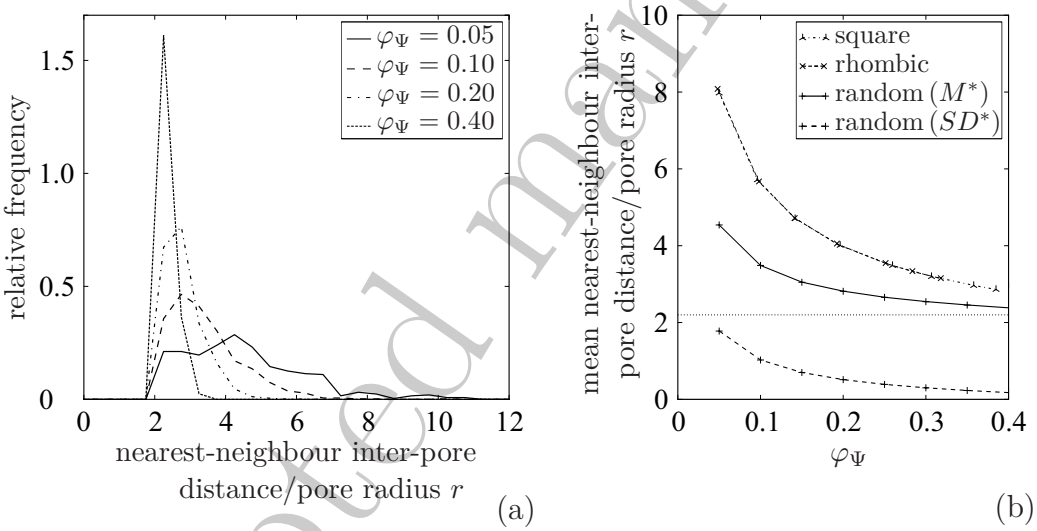

Figure 5: (a) Frequency polygons of the averaged nearest-neighbour inter-pore distances for RVEs with 5 %, 10 %, 20 % and 40 % porosity and random pore configurations. (b) mean nearest-neighbour inter-pore distances and standard deviations for square, rhombic and random pore configurations at different porosity levels (* averaged over 1000 random RVEs per porosity level). The dotted line marks the predefined minimum inter-pore distance.

The frequency polygons were obtained from the respective histograms, averaged over all five random RVEs generated for each porosity level. For low pore content $\varphi_\Psi = 0.05$, a broad distribution of nearest-neighbour inter-pore distances with a mean of approximately $4.5\,r$ can be observed, whereas

the high pore density at $\varphi_\Psi = 0.4$ leads to a narrow, peaked distribution with a mean of approximately $2.4\,r$, which is close to the predefined minimum distance of $2.2\,r$. The mean and standard deviation of a nearest-neighbour pore distribution may therefore serve as indicators of the overall porosity and the randomness of a pore configuration: Random configurations with low porosity exhibit a comparatively high ratio of mean nearest-neighbour inter-pore distance to pore radius and a large standard deviation, while high porosity levels or clustered pore configurations are marked by a comparatively low mean and standard deviation. Ordered square and rhombic pore configurations exhibit even higher ratios of nearest-neighbour inter-pore distance to pore radius for the same porosity level, as can be seen in Fig. 5(b).

In order to identify critical values of mean nearest-neighbour inter-pore distances and standard deviations for random pore configurations with different porosity levels, a Monte-Carlo simulation was performed: At each porosity level, the means and standard deviations of the nearest-neighbour pore distributions of 1000 random RVEs were computed and averaged. The results are plotted in Fig. 5(b).

4.3. Effect of matrix Poisson's ratio

According to both the SCM and the MT, the effective Poisson's ratio $\overline{\nu}$ as well as the effective shear modulus $\overline{G}$ are dependent on the Poisson's ratio ν_m of the matrix phase, cf. Eqs. (29), (32) and (30). In order to further investigate the impact of ν_m on the effective elastic properties, additional finite element analyses with different values of ν_m were carried out. For better comparability with the SCM and MT predictions, only RVEs with random arrangements of pores, which exhibit approximately isotropic material behaviour, were considered. At each level of porosity, one of the existing RVEs with random pore configurations was re-evaluated for both $\nu_\mathrm{m} = 0.1$ and $\nu_\mathrm{m} = 0.4$.

The results obtained by the application of the SCM are shown in Fig. 6. Dashed, solid and dash-dotted lines indicate the SCM predictions, and the symbols '$\circ$', '$+$' and '$\square$' mark the results of the numerical experiments for $\nu_\mathrm{m} = 0.1$, $\nu_\mathrm{m} = 0.22$ and $\nu_\mathrm{m} = 0.4$, respectively.

Fig. 6(b) shows that the resulting normalised shear modulus $\overline{G}/G_\mathrm{m}$ found from the numerical experiments exhibits a slight dependence on the matrix Poisson's ratio ν_m, as predicted by the SCM. Regarding the normalised Poisson's ratio $\overline{\nu}/\nu_\mathrm{m}$ plotted in Fig. 6(c), the different values of ν_m affect the agreement of the SCM and FEM results at higher levels of porosity.

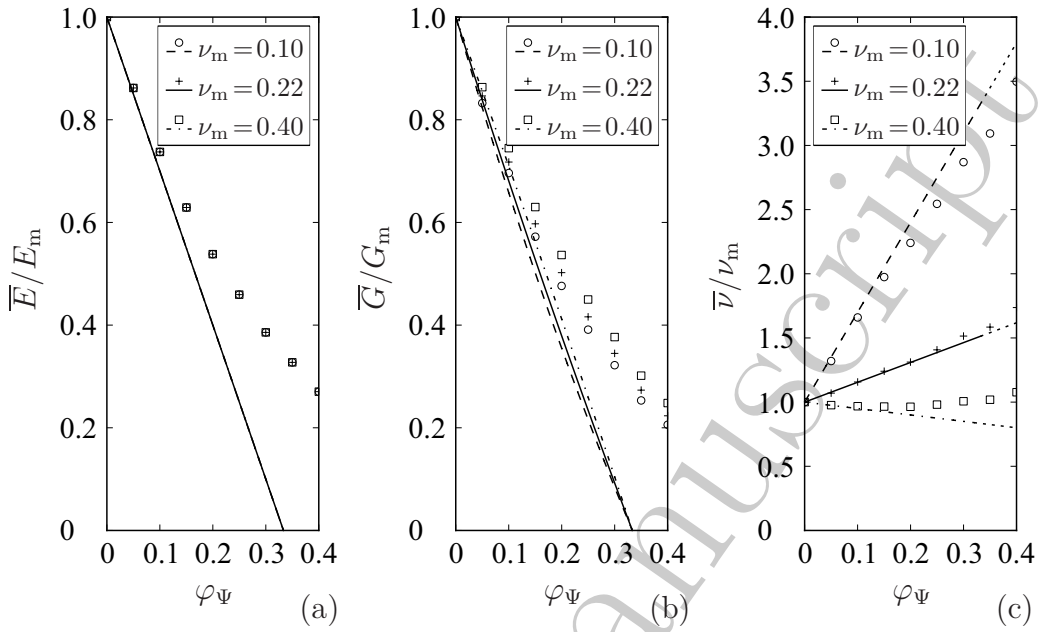

Figure 6: Comparison of the effective elastic properties obtained by the SCM and the FEM for RVEs with random pore configurations and different values of matrix Poisson's ratio ν_m.

The MT predictions and the FEM results are plotted in Fig. 7. With regard to the effective elastic moduli $\overline{E}/E_\mathrm{m}$ and $\overline{G}/G_\mathrm{m}$, the MT predictions show good agreement with the FEM results, even at higher levels of porosity. For the normalised Poisson's ratio $\overline{\nu}/\nu_\mathrm{m}$, however, the results of both approaches deviate considerably with decreasing matrix Poisson's ratio.

5. Conclusions

The effect of pore content, pore arrangement and inter-pore distance on the overall elastic response of planar RVEs with square, rhombic and random, non-clustered distributions of circular pores was studied by the classical self-consistent method (SCM), the Mori-Tanaka approach (MT) and the finite element method (FEM). The comparison of the effective elastic properties predicted by both the SCM and the MT with those obtained by the FEM demonstrates that the SCM and the MT provide viable and efficient alternatives to numerical models for the homogenization of porous media under plane stress conditions. The results show that Eqs. (28)–(32) may even be applied to the homogenization of RVEs with ordered pore

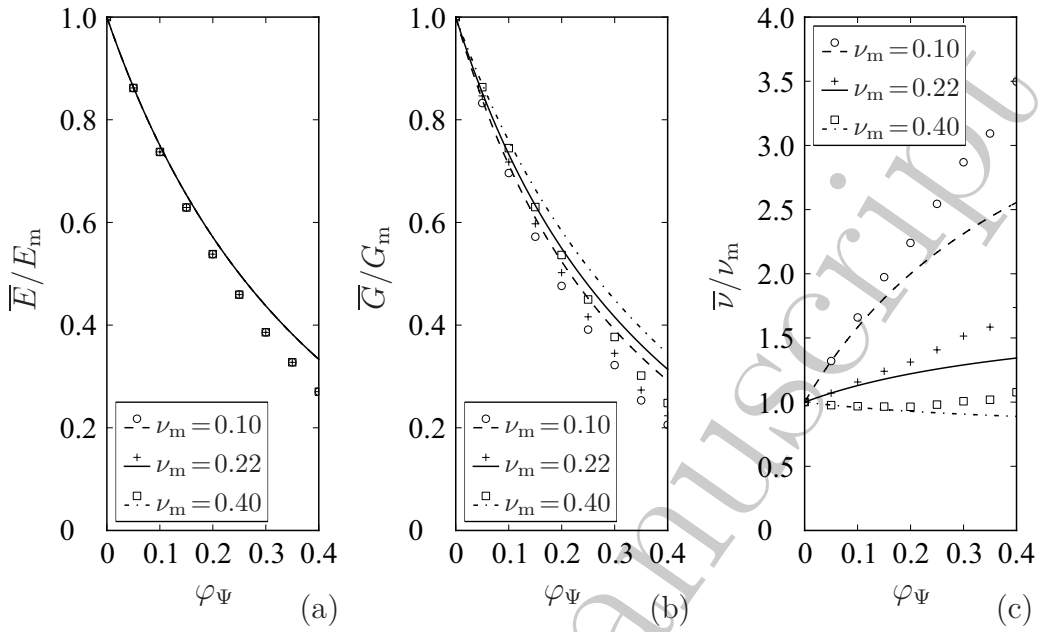

Figure 7: Comparison of the effective elastic properties obtained by the MT and the FEM for RVEs with random pore configurations and different values of matrix Poisson's ratio ν_m.

structure that exhibit overall orthotropic material behaviour, provided that pore content is low. The range of validity of the SCM and the MT for different pore arrangements can be defined as follows:

- For the square pore configuration, the SCM yields acceptable results for a porosity level of up to $\varphi_\Psi = 0.05$ or a minimum inter-pore distance of $8\,r$. The maximum relative difference between the results obtained by the SCM and the FEM is of the order of 3 %. Only the results for the effective shear modulus show slightly better agreement, with a maximum relative difference of approximately 7 % at $\varphi_\Psi = 0.14$.

  The MT predictions for the effective elastic moduli agree well with the FEM results for a porosity level of up to $\varphi_\Psi = 0.1$ or a minimum inter-pore distance of at least $5.7\,r$, the maximum relative difference being below 5 %. However, for the effective Poisson's ratio, the agreement of the results is less good.

- Similarly, for the rhombic pore configuration, the results obtained

by both the SCM and the FEM agree well up to a porosity level of $\varphi_\Psi = 0.05$ or a minimum inter-pore distance of approximately $8\,r$. At $\varphi_\Psi = 0.1$, the effective shear modulus predicted by the SCM already deviates from the FEM result by more than 10 %.

The MT predictions for the effective elastic moduli again show good agreement with the FEM results for a porosity level of up to $\varphi_\Psi = 0.1$, whereas the predicted effective Poisson's ratio deviates considerably from the FEM result at this porosity level.

- For random pore configurations, in contrast, the effective elastic properties predicted by the SCM match the FEM results well up to a porosity level of $\varphi_\Psi = 0.1$ or, for a sufficiently large number of pores, a mean nearest-neighbour inter-pore distance of at least $3.5\,r$. Over this porosity range, the predictions of the SCM for the effective elastic moduli deviate from the FEM results by at most 5 % at $\varphi_\Psi = 0.1$.

  The predictions obtained by the MT agree well with the FEM results for a porosity level of up to $\varphi_\Psi = 0.15$, the maximum relative difference being approximately 5.5 %.

The numerical experiments on random RVEs with varying matrix Poisson's ratio ν_m demonstrate that the effective Young's modulus $\overline{E}$ does not depend on ν_m. However, the effective shear modulus $\overline{G}$, and especially the effective Poisson's ratio $\overline{\nu}$, are influenced by variations in the Poisson's ratio of the matrix phase. Consequently, the concordance between the values of $\overline{G}$ and $\overline{\nu}$ predicted by both the SCM and the MT and those obtained by the FEM is affected as well: With regard to the SCM, the relative differences between the results are still well below 10 % over the aforementioned porosity interval [0, 0.1], irrespective of the matrix Poisson's ratio. At higher levels of porosity, the effect of ν_m on the SCM predictions for $\overline{\nu}$, which is also evident from Eq. (29), is more pronounced. For low matrix Poisson's ratio, the SCM tends to overestimate the effective Poisson's ratio computed by the FEM, whereas for high matrix Poisson's ratio, the opposite trend is found. In the case of the MT, the relative differences between the results are below 10 % over the porosity interval [0, 0.15]. Large deviations between the MT predictions and the FEM results occur primarily for the effective Poisson's ratio, which is generally underestimated by the MT for higher porosity levels.

These findings are of practical relevance for the homogenization of porous thin films and perforated layers, as well as for the evaluation of the in-

plane properties of cellular solids under plane stress conditions, and might, with limitations, even be used to estimate the effective properties of RVEs with random distributions of spherical pores, as discussed by Cojocaru and Karlsson (2010) and by Fiedler et al. (2010). The effective elastic properties of such materials can be conveniently predicted using both the SCM and the MT if their level of porosity lies within the stated intervals. For higher levels of porosity and overall shorter inter-pore distances, however, the SCM tends to underestimate and the MT tends to overestimate the effective elastic moduli obtained by the FEM.

References

Anthoine, A., 1995. Derivation of the in-plane elastic characteristics of masonry through homogenization theory. Int. J. Solids Struct. 32, 137–163.

Barai, P., Weng, G.J., 2011. Mechanics of a nanocrystalline coating and grain-size dependence of its plastic strength. Mech. Mater. 43, 496–504.

Ben-Nissan, B., Choi, A.H., Bendavid, A., 2013. Mechanical properties of inorganic biomedical thin films and their corresponding testing methods. Surf. Coat. Technol. 233, 39–48.

Benveniste, Y., 1987. A new approach to the application of Mori-Tanaka's theory in composite materials. Mech. Mater. 6, 147–157.

Bhushan, B., Venkatesan, S., 2005. Effective mechanical properties of layered rough surfaces. Thin Solid Films 473, 278–295.

Böhm, H.J., 2011. A Short Introduction to Basic Concepts of Continuum Micromechanics. Vienna University of Technology, ILSB, Vienna.

Buchko, C.J., Kozloff, K.M., Martin, D.C., 2001. Surface characterization of porous, biocompatible protein polymer thin films. Biomaterials 22, 1289–1300.

Budiansky, B., 1965. On the elastic moduli of some heterogeneous materials. J. Mech. Phys. Solids 13, 223–227.

Cabrillac, R., Malou, Z., Dumontet, H., 1998. Study of the influence of shape and orientation of the pores on the rigidity of porous materials through a homogenization method, in: Brebbia, C.A., De Wilde, W.P., Blain, W.R. (Eds.), Computer Methods in Composite Materials VI. WIT Press, Southampton, pp. 553–567.

Chao, K.-J., Liu, P.-H., Huang, K.-Y., 2005. Thin films of mesoporous silica: characterization and applications. C.R. Chim. 8, 727–739.

Cojocaru, D., Karlsson, A.M., 2010. On the effective properties of macroscopically isotropic media containing randomly dispersed spherical particles. J. Eng. Mater. Technol. 132, 021011-1–021011-11.

Dassault Systèmes, 2010. Abaqus FEA 6.10 Handbook. Providence, USA.

Day, A.R., Snyder, K.A., Garboczi, E.J., Thorpe, M.F., 1992. The elastic moduli of a sheet containing circular holes. J. Mech. Phys. Solids 40, 1031–1051.

Eshelby, J.D., 1957. The determination of the elastic field of an ellipsoidal inclusion, and related problems. Proc. R. Soc. London, Ser. A 241, 376–396.

Fiedler, T., Kim, H.S., Belova, I.V., Sloan, S.W., Murch, G.E., Öchsner, A., 2010. Elastic

finite element analysis on cross-sections of random hollow sphere structures. Mat.-wiss. u. Werkstofftech. 41, 250–256.
Flannery, C.M., Murray, C., Streiter, I., Schulz, S.E., 2001. Characterization of thin-film aerogel porosity and stiffness with laser-generated surface acoustic waves. Thin Solid Films 388, 1–4.
Föll, H., Christophersen, M., Carstensen, J., Hasse, G., 2002. Formation and application of porous silicon. Mater. Sci. Eng. R 39, 93–141.
Ha, T.-J., Park, H.-H., Kang, E.S., Shin, S., Cho, H.H., 2010. Variations in mechanical and thermal properties of mesoporous alumina thin films due to porosity and ordered pore structure. J. Colloid Interface Sci. 345, 120–124.
Hemmouche, L., Chicot, D., Amrouche, A., Iost, A., Belouchrani, M.A., Decoopman, X., Louis, G., Puchi-Cabrera, E.S., 2013. An analysis of the elastic properties of a porous aluminium oxide film by means of indentation techniques. Mat. Sci. Eng. A 585, 155–164.
Hershey, A.V., 1954. The elasticity of an isotropic aggregate of anisotropic cubic crystals. J. Appl. Mech. 21, 236–241.
Hill, R., 1963. Elastic properties of reinforced solids: Some theoretical principles. J. Mech. Phys. Solids 11, 357–372.
Hill, R., 1965. A self-consistent mechanics of composite materials. J. Mech. Phys. Solids 13, 213–222.
Hinrichsen, E.L., Feder, J., Jøssang, T., 1986. Geometry of random sequential adsorption. J. Stat. Phys. 44, 793–827.
Hu, N., Wang, B., Tan, G.W., Yao, Z.H., Yuan, W.F., 2000. Effective elastic properties of 2-D solids with circular holes: numerical simulations. Compos. Sci. Technol. 60, 1811–1823.
Huet, C., 1990. Application of variational concepts to size effects in elastic heterogeneous bodies. J. Mech. Phys. Solids 38, 813–841.
Jauffrès, D., Yacou, C., Verdier, M., Dendievel, R., Ayral, A., 2011. Mechanical properties of hierarchical porous silica thin films: Experimental characterization by nanoindentation and Finite Element modeling. Microporous Mesoporous Mater. 140, 120–129.
Khatam, H., Chen, L., Pindera, M.J., 2009. Elastic and plastic response of perforated metal sheets with different porosity architectures. J. Eng. Mater. Technol. 131, 031015-1–031015-14.
Kröner, E., 1958. Berechnung der elastischen Konstanten des Vielkristalls aus den Konstanten des Einkristalls. Z. Phys. 151, 504–518.
Kuiper, S., Brink, R., Nijdam, W., Krijnen, G.J.M., Elwenspoek, M.C., 2002. Ceramic microsieves: influence of perforation shape and distribution on flow resistance and membrane strength. J. Membr. Sci. 196, 149–157.
Markov, K.Z., 2000. Elementary Micromechanics of Heterogeneous Media, in: Markov, K.Z., Preziosi, L. (Eds.), Heterogeneous media: Micromechanics modeling methods and simulations. Birkhäuser, Boston, pp. 1–162.
Michel, J.C., Moulinec, H., Suquet, P., 1999. Effective properties of composite materials with periodic microstructure: A computational approach. Comput. Meth. Appl. Mech. Eng. 172, 109–143.
Mori, T., Tanaka, K., 1973. Average stress in matrix and average elastic energy of materials with misfitting inclusions. Acta Metall. 21, 571–574.

Morrell, R., 1985. Handbook of Properties of Technical & Engineering Ceramics. H.M.S.O., London.

Nemat-Nasser, S., Hori, M., 1999. Micromechanics: Overall Properties of Heterogeneous Materials, second ed. North Holland, Amsterdam.

Tanaka, K., Mori, T., 1972. Note on volume integrals of the elastic field around an ellipsoidal inclusion. J. Elasticity 2, 199–200.

Terada, K., Hori, M., Kyoya, T., Kikuchi, N., 2000. Simulation of the multiscale convergence in computational homogenization approaches. Int. J. Solids Struct. 37, 2285–2311.

Torquato, S., 2006. Random Heterogeneous Materials: Microstructure and Macroscopic Properties. Springer, New York.

Van Noyen, J., Mullens, S., Snijkers, F., Luyten, J., 2011. Catalyst design with porous functional structures, in: Reniers, G., Brebbia, C.A. (Eds.), Proc. of the 1^{st} Int. Conf. on Sustainable Chemistry. WIT Press, Southampton, pp. 93–102.

Vanstreels, K., Wu, C., Gonzalez, M., Schneider, D., Gidley, D., Verdonck, P., Baklanov, M.R., 2013. Effect of pore structure of nanometer scale porous films on the measured elastic modulus. Langmuir 29, 12025–12035.

Weng, G.J., 1984. Some elastic properties of reinforced solids, with special reference to isotropic ones containing spherical inclusions. Int. J. Eng. Sci. 22, 845–856.

Widom, B., 1966. Random sequential addition of hard spheres to a volume. J. Chem. Phys. 44, 3888–3894.

Xie, X.M., Fan, H., 2010. Effective modulus of heterogeneous materials in thin film configurations. Mat. Sci. Eng. A 527, 5452-5461.

Zander, N.E., Orlicki, J.A., Karikari, A.S., Long, T.E., Rawlett, A.M., 2007. Superhydrophobic surfaces via micrometer-scale templated pillars. Chem. Mater. 19, 6145–6149.

Zekry, J., Vandevelde, B., Bouwstra, S., Puers, R., Van Hoof, C., Tilmans, H.A.C., 2010. Thermomechanical design and modeling of porous alumina-based thin film packages for MEMS, in: Proc. of the 11^{th} Int. Conf. on Thermal, Mechanical & Multi-Physics Simulation and Experiments in Microelectronics and Microsystems. IEEE, New York, pp. 204–210.

Zhou, W., Bailey, S., Sooryakumar, R., King, S., Xu, G., Mays, E., Ege, C., Bielefeld, J., Yang, S., 2011. Elastic properties of porous low-k dielectric nano-films. J. Appl. Phys. 110, 043520-1–043520-8.

Zohdi, T.I., Wriggers, P., 2005. An Introduction to Computational Micromechanics. Springer, Berlin, Heidelberg.